# Directional effects during ion implantation:   Lateral mass transport and anisotropic growth

M. Chicoine, S. Roorda, and L. Cliche

*Groupe de Recherche en Physique et Technologie des Couches Minces (GCM), Département de Physique, Université de Montréal, C.P. 6128, Succursale Centre-Ville, Montréal, Québec H3C 3J7, Canada*

R. A. Masut

*Groupe de Recherche en Physique et Technologie des Couches Minces (GCM), Département de Génie Physique, École Polytechnique de Montréal, C.P. 6079, Succursale Centre-Ville, Montréal, Québec H3C 3A7, Canada*

In this paper we present experiments aimed at understanding three different phenomena that deform the surface of solids during irradiation by 24-MeV heavy ions. These phenomena are (1) density changes; (2) anisotropic growth, which describes the thinning of a solid along the normal to the surface and its growth in the surface plane without density changes; and (3) lateral mass transport. Lateral mass transport occurs only if the ion beam is no longer perpendicular to the surface. It consists of the displacement of some of the implanted material along the surface in the direction of the component of the ion velocity parallel to the surface; it results in the creation of a ditch and a dike at the opposite edges of the irradiated zone. The contribution of lateral mass transport to the surface deformation is deduced and studied as a function of ion fluence, flux, and species for a variety of projectiles and amorphous and crystalline materials such as InP, Si, SiO$_2$, and metallic glasses. Auger analysis of the surface discards sputtering and surface diffusion as possible causes of ditch and dike structures. A model based on the melting of the ion track by electronic stopping and on the shear stress applied to the target by momentum transfer of the ions is presented. [S0163-1829(97)05627-0]

## I. INTRODUCTION

It is now well established that energy losses of multi-MeV heavy ions via excitations and ionizations can induce damage and structural changes in solids, even in those with good electrical conductivity. For example, excitations and ionizations lead to permanent changes such as latent track formation in insulators and in conductors,[1] changes in electrical resistance and resistivity,[2,3] amorphization of metallic alloys,[4] and anisotropic growth effects.[5]

Damage formation due to atomic collisions is relatively well understood. Quantitatively, it can be fairly well predicted with programs like TRIM. However, the processes underlying damage formation by inelastic collisions still need to be clarified. Several models of damage formation by electronic excitation processes have been proposed in the literature. The ones better known are the thermal spike,[6] the Coulomb explosion,[7] and, more recently, the viscoelastic model.[8] Programs that evaluate radiation damage usually treat inelastic collisions only as a way of losing energy for the incoming ion. Neither the resulting momenta and trajectories given to the target ions and electrons are calculated nor is the resulting damage estimated.

In a recent paper,[9] it was shown that patches of InP were displaced laterally following off-normal, MeV ion implantation at liquid nitrogen temperature, as illustrated in Fig. 1. The figure shows the surface profile of InP after low temperature 7° off-normal irradiation by 24-MeV Se ions at a fluence of $5\times10^{14}$ ions/cm$^2$ through rectangular slits in a steel contact mask. Two atomic-force-microscopy pictures taken at the two different positions indicated on the surface profile are also shown. The valley and peak on the surface profile are in fact a ditch and a dike in three-dimensional

representation. Arrows indicate the direction of the incident ion beam. The valley on the left and the peak on the right are indicative of mass transport from left to right. The small peak on the left will be discussed later in this paper. The features exemplified in the figure combined with the fact that the direction of the mass transport always follows the direction of the off-normal component of the ion momentum suggests that lateral mass transport is related to the momentum (dimension and direction) of the incident ions.

One of the explanations that has been put forward is based on the transfer of momentum from the ions to the target.[9] As the ion is slowed down, it locally exerts a force on the solid, which responds by deforming itself. The ion beam literally
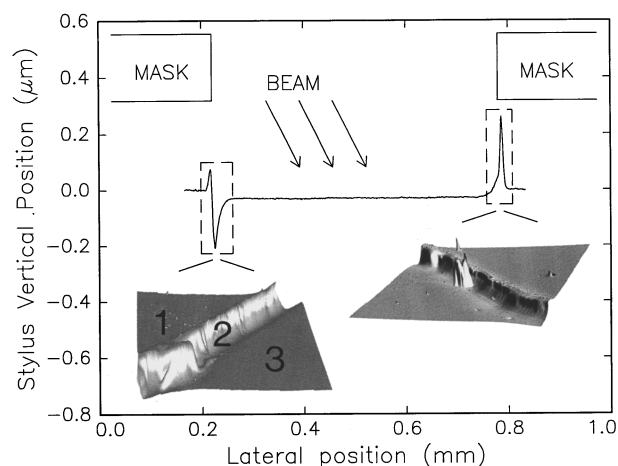


FIG. 1. Surface profile of InP after $5\times10^{14}$ ions/cm$^2$ Se 24-MeV irradiation at 7°. The two AFM figures correspond to the two rectangular boxes on the surface profile.

''pushes'' on the solid, thus creating a ditch on the windward side and a dike on the downwind side. In order for this to occur, the solid has to be deformable. Experimental work[10] shows that, during irradiation, strain can be relieved by viscous flow, and there is evidence from theoretical work in the nuclear[11] and electronic[6,12] collision regimes that during a few ps after the collision cascade, a small region around the ion track melts. It has been proposed[9] that macroscopic momentum transfer from the ion to the target occurs both in the nuclear and electronic energy loss regimes. It is known that microscopic momentum transfers through elastic collisions play an important role in radiation damage creation. In particular it is the way Frenkel pairs (interstitial-vacancy pairs) are created and separated. It has to be noted, however, that this microscopic momentum transfer (binary collisions between nuclei) cannot quantitatively account for the observed lateral mass transport: the effect is much larger than what would be expected if it was only due to elastic collisions.

Recent more detailed observations of macroscopic mass transport effects under ion bombardment will be presented in this paper. The surfaces of the implanted samples were modified by three different effects: (1) lateral mass transport, (2) ion-beam-induced densification, and (3) anisotropic growth. This third effect, also known as hammering or the Klaumünzer effect, is manifested as a growth of the sample dimensions perpendicular to the ion beam accompanied by a shrinking of the parallel dimension. In implantation experiments, all three effects occur simultaneously and cannot be observed independently. Basic attributes of each of these effects are the following:

(1) Lateral mass transport varies with the incident ion beam angle relative to the surface normal, according to a $\sin\theta\cos\theta$ dependence, where $\theta$ is the angle between the ion beam and the surface normal. The $\sin\theta$ factor reflects the fact that the effect depends on the off-normal component of the ion momentum, i.e., there is no lateral mass transport for $\theta = 0°$ because that component is zero. The $\cos\theta$ factor takes into account that when $\theta$ increases, the ion penetrates less deep into the sample. Lateral mass transport increases supralinearly with the energy of the incident ions, which has been explained with a simple model (see Ref. 9 and Sec. IV B) taking into account the total energy loss of the ion and radiation enhanced viscosity[10] in the sample. Finally the effect varies linearly with fluence and depends, amongst other things, on irradiation temperature, projectile mass, and the target used.

(2) In most materials, irradiation is accompanied by density changes. Unlike most crystalline semiconductors, InP compacts when irradiated by ions.[13,14] In its relaxed state, amorphous InP ($a$-InP) is found to be 0.17% more dense than crystalline InP ($c$-InP). It should be noted that during relaxation, $a$-InP *expands*. Hence relaxed $a$-InP can be compacted again if reirradiated. One way to avoid relaxation of compacted samples is to keep them at liquid-nitrogen temperature, where the relaxation rate is negligible. Other target materials may exhibit different density variations.

(3) It has been observed that during ion bombardment of amorphous metal alloys at several hundreds of MeV, thin films became larger but thinner as if they were between hammer and anvil, dubbed ''the anisotropic growth effect.'' It has been observed in several classes of amorphous materials including $a$-InP,[13] but never in crystalline materials. The effect increases as temperature decreases, and becomes observable only at temperatures well below room temperature.

After a brief examination of relevant experimental details in Sec. II, we will present our results in Sec. III. We will first study the behavior of $a$-InP when irradiated with 24-MeV ions at normal incidence, so that there is no lateral mass transport. Then, considering irradiations at off-normal angles, it will be shown using Auger electron spectroscopy that the valleys and dikes are not created by sputtering, and that lateral mass transport is not caused by surface diffusion phenomena.

The fluence dependence of lateral mass transport will be shown for both amorphous and initially crystalline InP. It will be inferred from these results that lateral mass transport only begins when InP becomes amorphous. The discussion in Sec. IV first describes a possible scenario for lateral mass transport, the role of momentum in mass flow and the similarities between lateral mass transport and anisotropic growth. We present our conclusions in Sec. V.

## II. EXPERIMENT

### A. Targets

Four different target materials were used: $a$-Si, fused silica, $a$-Fe$_{40}$Ni$_{40}$B$_{20}$ and InP. The Si, fused silica and $a$-Fe$_{40}$Ni$_{40}$B$_{20}$ samples, respectively, were taken from $p$-type $\langle 100 \rangle$ Si wafers, high-purity fused silica wafers (suprasil-2, Heraeus Amersil Inc.) and metglass 2826 ribbons (AlliedSignal Inc.). The metglass ribbons were polished until they had a mirrorlike surface. Three different kinds of InP samples, all of them obtained from semi-insulating InP(100) wafers were used: crystalline, relaxed ion amorphized samples, and similar but nonrelaxed material. The ion-amorphized samples are embedded at the surface of the crystalline wafer. The crystalline samples were taken directly from the wafer: they did not receive any pretreatment except cleaning and degreasing. The relaxed amorphized samples were first amorphized by ion implantation and were then left at room temperature for at least 20 days. During this time, almost all the density relaxation has occurred.[13] Nonrelaxed amorphous samples were kept in liquid nitrogen between their amorphization by ion implantation and further implantations, or else they were implanted immediately following the amorphization.

### B. Amorphization

For amorphization, small pieces ($4 \times 6$ mm$^2$) of $c$-InP and Si were first degreased and then clamped to a copper block using a thin intermediate layer of heat conductive paste to guarantee a good thermal contact. The InP (or Si) samples were uniformly implanted with $10^{14}$ cm$^{-2}$ (or $5 \times 10^{14}$ cm$^{-2}$ in the case of Si targets) Se ions at several energies (2, 3.6, 6, 10, 17, 24, and 30 MeV) in order to produce thick ($\approx 7$ $\mu$m) uniform amorphous surface layers. All the irradiations were conducted at $-180$ °C. The beam diameter was about 3 mm and it was scanned with scan frequencies of 64 Hz vertically and 517 Hz horizontally over a 1-cm$^2$ surface. The angle between the ion beam and the sample holder was set to $\approx 7°$ in order to minimize channel-
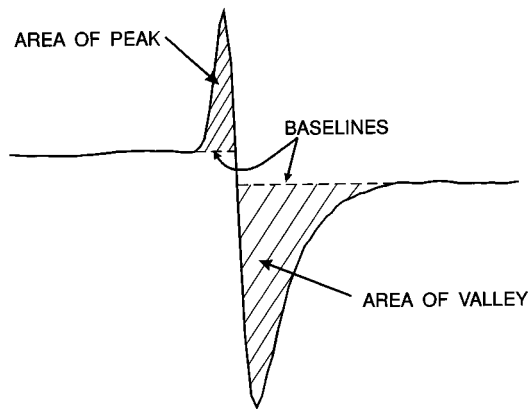
FIG. 2. Example of a surface profile. The number of displaced atoms along 1 cm is calculated from the dashed areas.



FIG. 3. AFM picture of an unrelaxed amorphized InP sample irradiated at normal incidence by 24-MeV $5 \times 10^{15}$ Se ions/cm$^2$.

ing. Raman spectroscopy was used to verify that the near surface of InP is indeed amorphous after 2-MeV, $10^{14}$-cm$^{-2}$ Se implantation. In order to verify that the amorphization was continuous, one amorphized sample was beveled. Raman spectroscopy on different spots on the beveled surface, corresponding to different depths in the sample, confirmed that the whole layer was amorphous.

### C. Irradiation

The $a$-SiO$_2$, $a$-Fe$_{40}$Ni$_{40}$B$_{20}$, and amorphized Si and InP samples were then irradiated with 24-MeV Se ions with a steel contact mask placed directly on top, in order to produce alternating implanted and nonimplanted regions. No special treatment to remove the oxide layer on the surface of the samples was considered necessary because its thickness is negligible compared to the dimensions of the observed structures. Different angles (0° and 7°) between the beam and the surface normal were used. The precision in the angle value was about 0.1°. To evaluate the dose precisely, the beam current was measured with a beam profile monitor which was calibrated against a Faraday cup. It was necessary to do so because direct measurement of the current on the target is altered by secondary electron emission.

### D. Profilometry and evaluation of peak surfaces

The implanted surfaces were characterized with a Dektak 3030ST stylus profilometer. Each profile of the masked surface, which gives a cross section of the studied structures, covered at least one complete period of alternating bombarded and unbombarded regions. The intrinsic curvature of the samples can be subtracted from the profiles by using a polynomial fit. In order to evaluate the amount of matter that was displaced, the surface area of each peak or valley was calculated. Figure 2 shows an example of a typical part of a surface profile. For each peak or valley shape, the baseline was set to coincide with the level of the adjacent unbombarded surfaces. Then the curve of the peak or valley shape was integrated to obtain the area. This area was multiplied by the total length of the structure to obtain the volume which was expressed in number of atoms using the atomic density of the material. This assumes translational symmetry along a line perpendicular to the plane of the figure, which is nor-
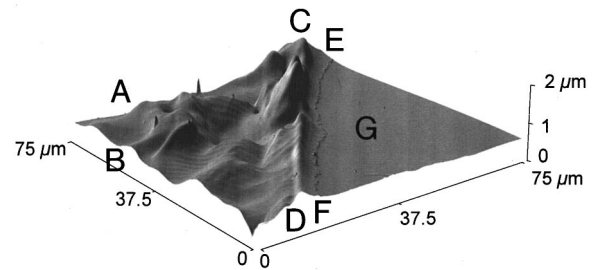
mally true except for irradiations at normal incidence, as will be seen in Sec. III A. The data points which will be presented are the mean values of usually six calculated areas, and the corresponding errors are the standard deviations of these values.

### E. Atomic force microscopy

Atomic force microscopy (AFM) was performed with a Topometrix Discoverer TMX2010 machine in the contact mode using a pyramidal tip. The dimensions of the scanned areas were $75 \times 75$ $\mu$m$^2$ with a 0.375-$\mu$m lateral resolution. The linear scan velocity was 200 $\mu$m/min. It has been verified by direct comparison that the picture treatment used to give a three-dimensional representation, such as shadowing and coloring, did not introduce any artifacts. Dektak traces could be seen on some of the AFM pictures. These traces were uniform and continuous even when crossing deep valleys and high peaks, confirming the reliability of the profilometry presented in this work.

### F. Auger electron spectroscopy

Auger electron spectroscopy was performed with a JEOL JAMP-30 Scanning Auger Microscope on 24-MeV Se irradiated $c$-InP samples covered by a 50-nm gold layer in order to verify that this layer is not sputtered by the ion beam. The electron acceleration voltage was 5 kV. Depth profiles were taken simultaneously at three points on the sample. For the depth profiles, the surface was etched by a 3-keV Ar beam during 20 s between each scan.

### III. RESULTS

### A. Irradiation at normal incidence

The simplest irradiation geometry that can be used is irradiation at normal incidence. In this configuration there can be no lateral momentum induced mass transport. The only effects that should be observed are anisotropic growth and density changes. Figure 3 shows an AFM picture of a preamorphized, nonrelaxed InP sample. A mask was placed on top of the sample during irradiation at normal incidence with 24-MeV Se ions at a fluence of $5 \times 10^{15}$ ions/cm$^2$. Line $EF$ marks the frontier between irradiated and nonirradiated parts. It is emphasized that roughness as shown in this picture occurs only at the borderline between masked and unmasked material. Other images taken at the same scale and away from the borderline, either on the masked or unmasked area, show a completely featureless surface. One may realize

that the flat part of Fig. 3 was already implanted (without any mask at all) when the sample was preamorphized. This underlines that the corrugations shown in the figure occur only at the edges of the mask. The implanted region is depressed by about 170 nm compared to the nonimplanted region. The corrugated region has three different features. First there is an undulating band about 40 $\mu$m wide between lines $AB$ and $CD$. This region is made of scattered peaks and valleys of up to 300–500 nm deep or high. Next there is a $\approx 10$-$\mu$m-wide dike along line $CD$. This dike, although varying in height and width, has a much more regular topology than the region along line $AB$. Its height varies between about 300 and 1000 nm. Finally there is a step along line $EF$. The step height between this step and $G$, the nonimplanted region, is $\approx 170$ nm. These transformations of the InP surface are a result of the anisotropic growth effect. When the region uncovered by the mask is irradiated, it tends to become thinner and larger, thus exerting stress on the surrounding material, that is, the regions covered by the mask. Then the material at the edges of the slits relieves this stress by flowing out of plane by plastic flow, forming the dike. Considering the irregularity of the shapes observed, it appears that plastic flow out of the plane is triggered by random events.

The step between line $EF$ and region $G$ is thought to be due to plastic deformation of the nonirradiated part of the InP substrate. The stress created at the edge of the irradiated area is mostly relieved by plastic flow of irradiated InP, but a part of this stress could also be accommodated by the deformation of the nonirradiated InP, resulting in the step observed along line $EF$. A similar type of deformation was observed in silicon,[15] and in that case it was found that the plastic flow in the crystalline material was mediated by dislocations.

### B. Absence of sputtering and surface diffusion

From now on, only off-normal irradiations will be considered. Features similar to those observed in Fig. 1 have been observed in keV irradiations (an energy range where sputtering rates are at a maximum) where the observed valleys would be due to sputtering enhanced by edge effects. Auger spectroscopy was used to verify that the structures observed in this work are not due to sputtering; it has been shown elsewhere[9] that the peak shapes are not created by mask deposition. A thin gold layer ($\approx 50$ nm) was deposited on the surface of a $c$-InP sample. The sample was then irradiated at 7° with 24-MeV Se ions at a fluence of $5 \times 10^{14}$ ions/cm$^2$ through a contact mask. At the windward side of the mask, this results in a 65-nm-deep valley. If the valley were formed by sputtering, the gold layer, thinner than 65 nm, would have to be completely eroded. Figure 4 shows the Auger depth profiles taken at the three different locations like the ones respectively shown on the left AFM picture in Fig. 1. The $y$ axis shows the signal intensity and the $x$ axis shows the sputtering time. Profile 1 was taken on the masked region (region 1 in Fig. 1), 2 was taken at the bottom of a valley, and 3 was taken at an unmasked but flat region (region 3 in Fig. 1). These profiles show that the thickness of the gold layer did not vary much, even at the bottom of the valley, and therefore the valley was not sputtered.
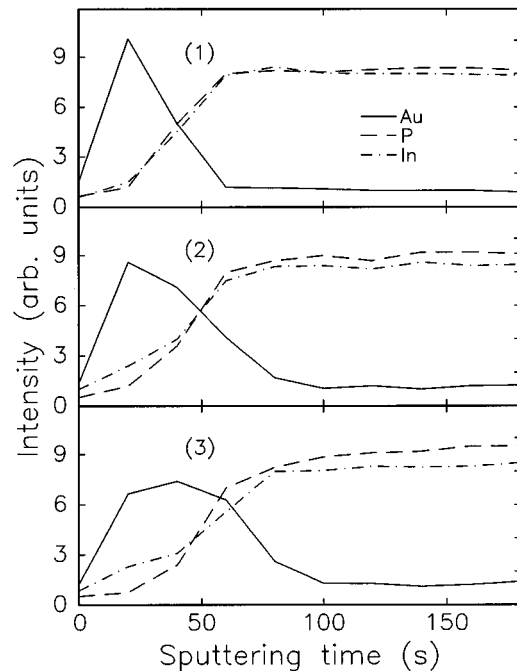


FIG. 4. Auger depth profiles taken at the three locations shown in Fig. 1.

Besides discarding sputtering as a cause for the formation of the valleys, this analysis indicates that lateral mass transport is not a surface diffusion phenomenon. Under irradiation, the gold atoms at the surface could acquire a mobility sufficient to allow them to move on the surface. But again in that case there would be no gold left in the valley, contrary to Auger observations.

It is interesting to note that in panels 2 and 3 of Fig. 4, the interface between Au and InP appears less sharp than in panel 1 (the masked region). This would be indicative of some ion beam mixing, which is brought about as a result of the electronic stopping, since the nuclear stopping at the surface is negligible for 24-MeV Se.

### C. Fluence dependence of lateral mass transport

The evolution of the sample surface structure with increasing ion fluence for irradiations at fixed angle and energy will now be considered. Figure 5 shows the morphology of InP samples bombarded by 24-MeV Se ions at an angle of 7° as a function of fluence. The orientation of the beam is the same as in Fig. 1, and the profiles are all oriented the same way with respect to the beam. The figure shows different Dektak profiles of sample surfaces, each one covering a region corresponding to a complete slit of the contact mask. The profiles on the left of the figure correspond to crystalline samples bombarded at different fluences (0.5, 1, 5, and $10 \times 10^{14}$ at./cm$^2$). The profiles on the right correspond to previously amorphized and relaxed samples irradiated at the same fluences. On each profile, a small peak appears at the extreme left, whose magnitude does not vary much with fluence $A$. Just at the right of this peak a valley appears ($B$) whose depth is seen to increase with increasing fluence, both for amorphous and initially crystalline samples. At the extreme right of the profiles a peak appears ($C$) whose magni-
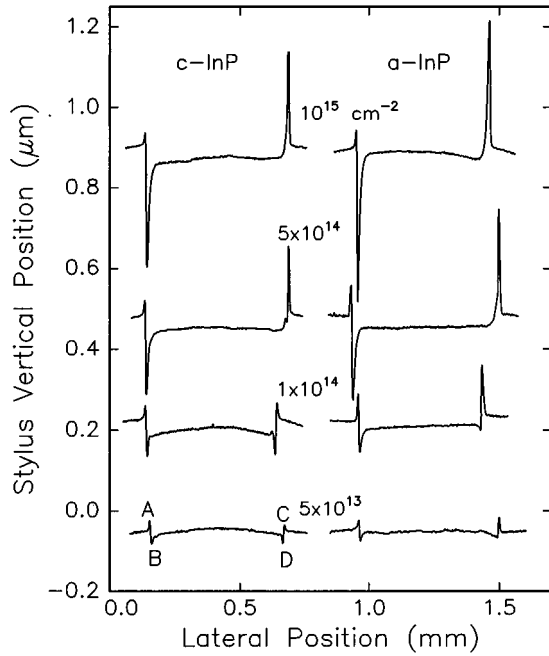
FIG. 5. Surface profiles of $c$-InP on the left and $a$-InP on the right irradiated by 24-MeV Se ions at various fluences.
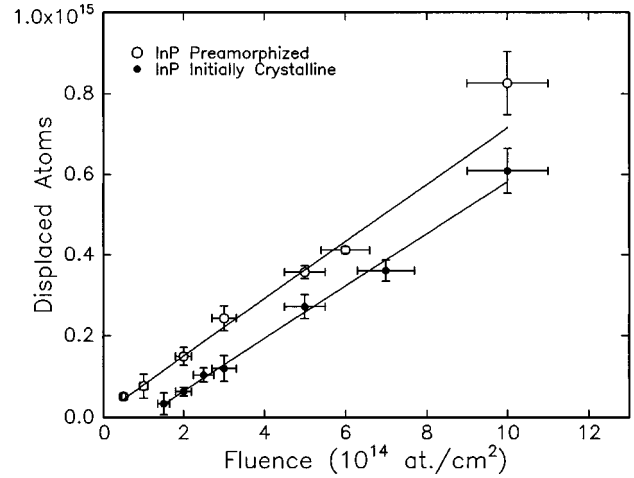


FIG. 6. Number of displaced atoms along 1 cm by 24-MeV Se ions as a function of fluence for preamorphized InP (empty circles) and initially crystalline InP (full circles) targets. The lines are linear least-square fits.

tude also increases with increasing fluence. And finally, just to the left of $C$ peaks, a shallow valley ($D$) can be seen on three crystalline (0.5, 1, and $5 \times 10^{14}$ at./cm$^2$) and two amorphous (0.5 and $1 \times 10^{14}$ at./cm$^2$) samples.

Let us consider peaks $C$ and valleys $B$. As explained in Sec. I, these structures are indicative of lateral mass transport. Figure 5 shows that the area of their cross sections increases with fluence: it is a cumulative effect. This effect is asymmetric in the sense that it creates a valley to the left of the implanted region, and a peak to the right. The amount of matter taken from $B$ equals the amount of matter that goes to $C$. The equivalent cross section of this amount of matter will be denoted by the letter $T$.

Next consider anisotropic growth. The consequence of this effect is the growth of the irradiated region in the plane of the target surface. As was already discussed in Sec. III, the grown material then flows out of the surface plane at the boundaries of the irradiated region. The evolution with fluence of this effect must be separated in two stages. The first stage goes on until the valley $B$ becomes so important that further anisotropic growth cannot reach the peak $A$. This peak then ceases to grow. The area of the cross section peak $A$, which is equal to the area of peak $C$ at low fluence, will be denoted $H_V$ the visible part of anisotropic growth. At this fluence, anisotropic growth has created two identical peaks of area $H_V$ on both sides of the irradiated region. The second stage then begins. Anisotropic growth goes on but it would now fill in valley $B$ instead of making peak $A$ grow. The growth of valley $D$ and peak $C$ does not change from one stage to the other.

The amount of matter that is transported must be deduced from the profiles. It can be extracted from the different peaks and valleys that form the profiles. Valley $B$ is dug by compaction and lateral mass transport and is filled in by hammering. The area of its cross section is thus given by

$$A_B = C + T - H_I, \tag{1}$$

where $C$ and $T$ represent the areas of the cross sections of the parts of the valley due to compaction and the lateral mass transport respectively, and $H_I$ represents the invisible filling in due to hammering subsequent to $H_V$. The sign convention is the following: a plus ($+$) means the effect contributes to the formation of the structure (here $C$ and $T$ contribute to the creation of valley $B$), and a minus ($-$) means the effect inhibits the formation of the structure (as $H_1$ does for valley $B$). Next there is peak $C$ which is due to a competition between lateral mass transport and hammering, spilling material over the edge of the implanted zone and compaction which creates a valley at the same location. It is also formed by the initial hammering peak which is the same as the windward peak, noted $H_V$. The area of its cross section is thus given by

$$A_C = T + H_I + H_V - C. \tag{2}$$

So from these two equations, the amount of matter transported laterally is found to be given by

$$T = \tfrac{1}{2}(A_B + A_C - H_V). \tag{3}$$

Calculating $T$ for a number of irradiations allows us to evaluate the evolution of the amount of lateral mass transport with ion fluence. Some data are shown in Fig. 6 for both $a$-InP (the upper line) and initially crystalline InP (the lower line). The vertical axis represents the number of displaced atoms, and the horizontal axis represents the fluence. The lines are linear least-square fits of the data. The lines have the same slopes within the error bars. The line for $a$-InP crosses the origin (within error bars) while the line for $c$-InP has an offset of $\approx 10^{14}$ ions/cm$^2$, which is about the amorphization fluence. This clearly shows that lateral mass transport only affects amorphous materials.
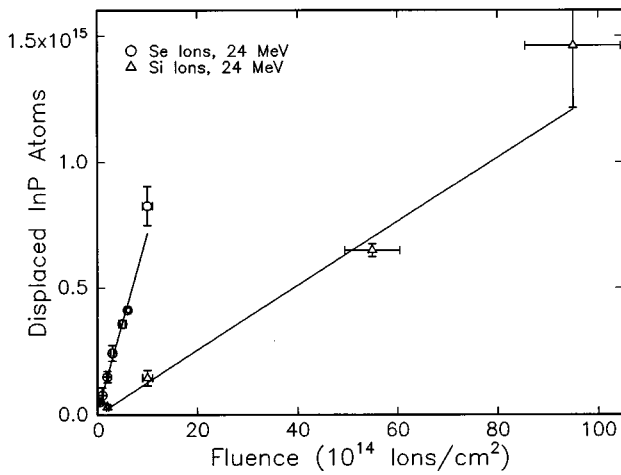
FIG. 7. Number of displaced atoms along 1 cm for Se (empty circles) and Si (triangles) ions as a function of fluence. Preamorphized InP samples were implanted with 24-MeV ions at an off-normal angle of 7°. The lines are linear least-square fits.

### D. Other targets and projectiles

The results on lateral mass transport presented so far were obtained with Se-irradiated InP. The effect of different projectiles on relaxed $a$-InP and Se ions on different targets as a function of fluence was also studied. The results are presented in Figs. 7 and 8. The incidence angle was 7° for both figures.

Figure 7 shows the number of displaced atoms as a function of fluence for 24-MeV $Se^{6+}$ and $Si^{4+}$ ions on $a$-InP irradiated at 7°. The ratio of the magnitudes of the effect for these different curves is given by the ratio of the slopes. It can be seen that lateral mass transport is about 5.5 times more efficient with Se ions than with Si ions. Figure 8 shows the number of displaced atoms as a function of fluence for 24-MeV Se ions on $a$-SiO$_2$, $a$-InP, $a$-Fe$_{40}$Ni$_{40}$B$_{20}$, and $a$-Si. The effect is strong for silica and very weak for Si targets.

It has been verified that lateral mass transport does not depend on ion flux for different values of beam current for
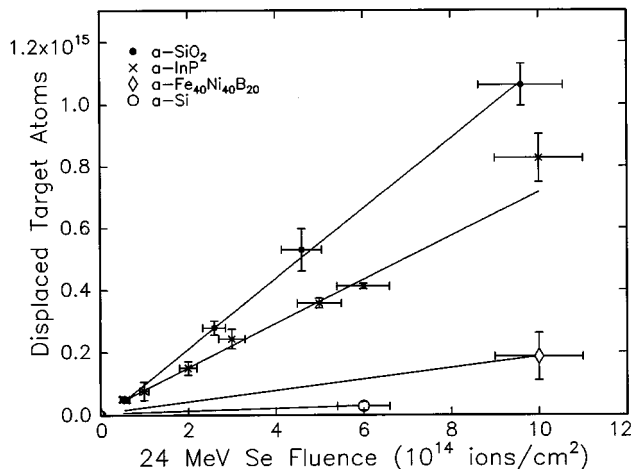


FIG. 8. Number of displaced atoms along 1 cm for $a$-InP (full circles), $a$-SiO$_2$ (crosses), $a$-Si (empty circles), and $a$-Fe$_{40}$Ni$_{40}$B$_{20}$ (lozenges). The lines are linear least-square fits.

$3 \times 10^{14}$-cm$^{-2}$ 24-MeV $Se^{6+}$ on $a$-InP at 7°. For the beam current range studied (10–115 nA), the effect was independent of flux. It was also verified that the number of displaced atoms for $10^{15}$-cm$^{-2}$ 24-MeV $Si^{4+}$ ions on $a$-InP and on $a$-Si was independent of the beam current in the 30–150-nA range.

## IV. DISCUSSION

### A. Scenario for lateral mass transport

The scenario proposed to explain lateral mass transport will be described in this section. The effect of momentum transfer will also be estimated. We distinguish three separate steps occurring simultaneously to explain lateral mass transport: creation of a liquid track by the ion, momentum transfer from the ion to the liquid track resulting in its deformation, and, finally, quenching of the deformed liquid.

In the electronic stopping regime, incoming ions eject electrons from atoms in the solid. The term ''ejected'' means ejected from an atom in the solid, not ejected from the solid itself. About half of the energy is lost in close collisions between the ion and the electrons, the other half being lost in resonant energy transfer to electrons far from the core of the ion track.[16] Only the energy lost in close collisions will contribute to liquefaction of the track. The trajectory of the electrons ejected from atoms is almost perpendicular to the ion trajectory, but, of course, the vectorial sum of the momenta given to the electrons must be equal to the momentum lost by the ion. The electrons that can be ejected (excitable electrons) are those having orbital velocities lower than the ion velocity (Bohr criterion for the number of excitable electrons). The energy transferred to an electron is given by

$$T = \left(\frac{1}{4\pi\varepsilon_0}\right)^2 \frac{2Z_1^2 e^4}{b^2 m v^2}, \tag{4}$$

where $b$ is the impact parameter of the collision, $\varepsilon_0$ the vacuum permittivity, $m$ the electron mass, $v$ the velocity of the ion, and $Z_1$ its effective charge, given by the Northcliffe formula: $Z_1 = Z[1 - \exp(-0.92v/(v_0 Z^{2/3}))]$, where $Z$ is the atomic number and $v_0$ the Bohr velocity. The minimum value of $b$ is chosen such that $T$ corresponds to the energy transferred to the electron in a head-on collision, that is, $b_{min} = Z_1 e^2/(4\pi\varepsilon_0 m v^2)$. The maximum value of $b$ is chosen such that $T$ corresponds to $I$, the mean atomic excitation energy of the excitable electrons, that is, $b_{max} = 2Z_1 e^2/[4\pi\varepsilon_0 (2m v^2 I)^{1/2}]$. From this information, it is straightforward to calculate the initial velocity distribution of the electrons.

As the electrons move through the solid, they lose their energy and thus distribute the energy lost initially by the ion over a larger region. The size of this region can be estimated using the range of fast electrons in the solid, and the point of origin and direction of each fast electron. This range can be expressed[17] as $R = (0.064/\rho)E_0^{1.68}$, where $R$ is the range in microns, $\rho$ is the material density in g/cm$^3$, and $E_0$ is the electron energy in keV. Once all the ingredients are known (transferred energy, number of excitable electrons, range of the electrons), the distribution of the deposited energy can be estimated. For this purpose, the range of an electron from the center of the ion track, noted $r$, as a function of the impact
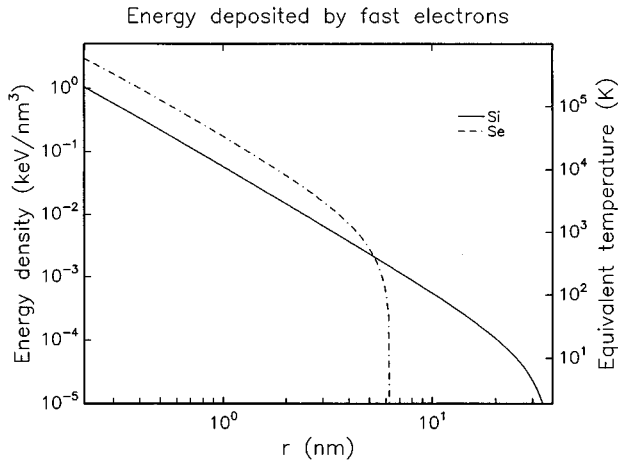
FIG. 9. Density of energy deposited by excited electrons as a function of distance from the track center for 24-MeV Se and Si ions in an InP target. On the right axis a temperature ''equivalence'' for the lattice atoms is shown.

parameter is first calculated, assuming that the electrons are ejected perpendicularly from the center of the ion track. This gives the range of impact parameters for which electrons cross a certain radius. Moreover, to each value of the impact parameter corresponds an electron energy and the number of electrons having received this energy. The total-energy density taken from one given impact parameter is spread over a disc of radius $r$. The final energy density at $r$ is found by integrating the total energy density as a function of impact parameter over the relevant impact parameter range. The result of this calculation for 24-MeV Se and Si ions in $a$-InP is presented in Fig. 9. It shows the density of energy deposited by the ejected electrons as a function of the distance from the center of the track after the passage of one ion. A temperature ''equivalence'' is shown on the right vertical axis assuming the deposited energy density to be equal to that of the lattice atoms with an energy of $\frac{3}{2}k_B T$ per atom. It can be calculated that 97% of the energy deposited by the electrons is initially concentrated in a small cylinder of no more than 3 nm for Se and 5 nm for Si ions (but see below). However, this is probably an overestimation of these radii, since the electrons lose their energy mostly by plasmon emission. In the context of high excitation density, the plasmon frequency, given by $\omega_p = (e^2 n/\varepsilon_0 m)^{1/2}$, where $n$ is the free-electron density, is increased substantially and thus the mean free path of electrons is decreased. The consequence is that the radii of the cylinders in which the electron energy is initially deposited is even smaller than the values taken from Fig. 9.

Concerning the narrowness of the cylinder in which the energy is deposited, it is pointed out that we evaluated exchanges within the electronic system only. The problem of the transfer of energy from the excited electrons to the lattice ions has also been considered by Toulemonde, Dufour, and Paumier within the thermal spike model.[6] In this model it is assumed that a temperature can be defined for the subsystem of the excited electrons and that the energy transfer is driven by electron-phonon interactions.[17] The temperature increase in the solid is calculated by solving the coupled heat equations for the ionic and electronic subsystems. The energy

transfer results in temperatures that can be high enough to melt and even vaporize the lattice. The temperature distribution is then used to estimate the radius of the liquefied track.

The effect of momentum transfer to the target can be estimated from the initial energy distribution of Fig. 9. Each atom receives a momentum proportional to the square root of the local energy deposition. The total momentum thus distributed must then be equal to the momentum lost by the incoming ion. Even if the trajectory is almost normal to the ion trajectory, it must have a component in the direction of the ion. The distribution of the momentum in the direction of the ion trajectory as a function of $r$ is assumed to scale with the total momentum per atom distribution deduced from the curve of Fig. 9. A velocity can then be attributed to each atom affected by the passage of the ion. The total displacement is obtained by multiplying this velocity by a displacement time. For 24-MeV Se ions in $a$-InP incident at 7°, each ion displaces the equivalent of $5.4 \times 10^6$ atoms over 1 nm.[9] If momentum transfer from the ion beam to the solid is the only mechanism responsible for lateral mass transport, the required displacement time estimated by comparing our calculation with the measured displacement is about 300 ps.

Given that the solidification velocity of the liquid-solid interface in InP is not known, it is difficult to assess whether atoms in the liquid InP column can move freely for 300 ps before solidification occurs. In this regard, Si has been studied in much more detail and the solidification velocity of the liquid-solid interface is known to be kinematically limited. No matter how fast the heat is transported away from the interface, limits to the interface velocity are 15 m/s for $c$-Si and 15 m/s (theory[18]) or 20 m/s (experiment[19]) for $a$-Si. The complete resolidification of a liquid cylinder of 10-nm radius would take at least 500 ps in $a$-Si, and presumably even more in $a$-InP. In an earlier published estimate,[9] the value $\Delta t = 1$ ps was assumed for the duration of the liquid track. Such a short duration now appears insufficient to account for lateral mass transport caused by momentum transfer.

If the target is crystalline, the deformed liquid would recrystallize by epitaxy and go back to its original form. Apparently, in an amorphous matrix the liquid track can solidify, retaining its deformed shape. The observed final deformation would be the superposition of all the small deformations caused by single-ion impacts, with a threshold fluence given by the fluence necessary for individual tracks to overlap and thus cover up the whole irradiated region. Assuming a track diameter of 5 nm, the threshold fluence would then be about $10^{12}$ ions/cm$^2$. The uncertainties of our experiments are too high to allow the verification of the validity of that number.

### B. Momentum transfer effect on mass flow

The energy dependence of the number of atoms that are displaced from the windward side to the downwind side by lateral mass transport can also be estimated. The ion track will be assumed to immediately liquefy with the passage of the ion as this occurs in a time scale small compared to the duration of the liquid track. This assumption is reasonable in the light of the results of the preceding section. The geometry of the calculation is described schematically in Fig. 10.
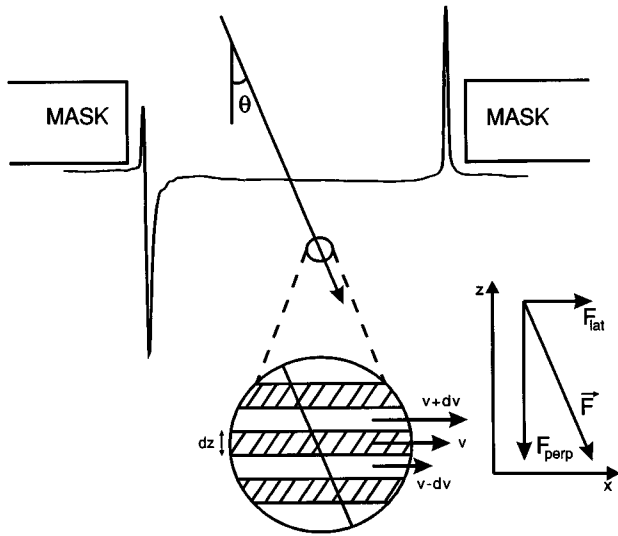
FIG. 10. Geometry of the calculation presented in Sec. IV B. The force **F** is exerted on a small liquid region of the target when an ion passes through it. The lateral component of this force gives the lateral velocity $\nu(z)$ to the different layers of material.

The ion is assumed to apply an instantaneous force $F$ equal to its energy loss, and which varies with depth $z$. Only the force component in the plane of the surface gives a lateral velocity $\nu(z)$ to the different layers of material. The force is assumed to be constant for the time $\Delta t$, the duration of the liquid track, and then to fall abruptly to zero. The total displacement as a function of depth for the affected atoms is then given by $\xi(z) = \Delta t \nu(z)$. The relation between $\tau_{\text{lat}}$, the shear stress applied by the ion beam and $\nu_{\text{lat}}$, the resulting velocity distribution is given by[20]

$$\tau_{\text{lat}} = \eta \, \frac{\partial \nu_{\text{lat}}}{\partial z}, \tag{5}$$

where $\eta$ is the radiation enhanced viscosity, $z$ is the depth, and $\nu_{\text{lat}}$ is the lateral velocity imparted to the host atoms. This equation describes the lateral velocity distribution as a function of depth that is given to a viscous material when a lateral shear stress is applied. The magnitude of the force furnished by the ion beam is $S_e + S_n$, the sum of electronic and nuclear energy losses, and the lateral stress at depth $y$ is thus

$$\tau_{\text{lat}} = \frac{\sin\theta \, \cos\theta}{A} \, (S_e + S_n), \tag{6}$$

where $\theta$ is the incident angle between the ion beam and the surface normal, and $A$ is the area of the ion track. For the viscosity, we take a liquidlike model

$$\eta = C \, \exp\left(\frac{E_a}{k_B T}\right), \tag{7}$$

where $C$ and $E_a$ are parameters that are fitted to experimental curves, and $k_B T$ is the temperature of the ion track. For the purpose of this simple calculation, the radial temperature distribution in Fig. 9 is simplified to a constant inside a cylinder of radius $A$ around the ion track, that is, $\frac{3}{2}k_B T = (nA)^{-1} (S_e + D_n)$, where $n$ is the atomic density of the

target and $A$ is the cascade cross section area. Equation (5) is integrated to obtain the instantaneous lateral velocity of each layer of material:

$$\nu(z) = \int_0^z \frac{\tau_{\text{lat}}}{\eta} \, dz' = \frac{\sin\theta \, \cos\theta}{CA} \int_0^z (S_e + S_n)$$

$$\times \exp\left(-\frac{2nAE_a}{3(S_e + S_n)}\right) dz'. \tag{8}$$

Then, assuming that $\nu(z)$ is constant over a time $\Delta t$, and after which it falls abruptly to zero, the mean displacement is

$$\bar{\xi} = \frac{1}{R_P} \int_0^{R_P} \xi(z) \, dz = \frac{\Delta t}{R_P} \int_0^{R_P} \nu(z) \, dz, \tag{9}$$

where $R_P$ is the projected range of the ion. The number of atoms directly affected is $nR_PA$, and $D$, the number of atoms displaced by lateral mass transport times the mean displacement, can be written

$$D = N_i(nR_PA)\bar{\xi}, \tag{10}$$

where $N_i$ is the number of ions that strike the surface.

The validity of Eq. (5) requires that a steady state has been established. In order for this assumption to be valid, $\Delta t$ must be much greater than the time needed to reach the steady state, which can be estimated to be of the order of $10^{-13}$ s, the thermalization time of the lattice. A fit of the theoretical values predicted by Eq. (10), with $\Delta t/(AC)$ and $AE_a$ considered as independent fit parameters, leads to the values for these parameters. Then values for $\Delta t$, the time for which the momentum transfer is effective, and $A$, the cascade cross-section area, can be estimated and used to determine a range of values for the viscosity. This model has been used to explain the energy dependence of lateral mass transport.[9] Although it explains the energy dependence better than alternative models based on momentum transfer, it is not yet sophisticated enough to explain the dependence of the effect on the projectile mass as observed in Fig. 7. This model can qualitatively predict that the effect is more pronounced for Se ions than for Si ions, as can be inferred from Fig. 9, but not the factor 5.5 observed when the same free parameters values are used for both ions. Figure 9, however, gives a hint about the origin of this problem. It is seen that the Si ion initially spreads its energy much farther (over a $\approx 35$-nm radius) than the Se ion, which initially spreads its energy over a $\approx 7$-nm radius. That would imply that more energy is deposited outside the liquid track for the Si ion, and thus that a smaller fraction of its energy is effectively available for lateral mass transport.

### C. Common origin for lateral mass transport and anisotropic growth

Anisotropic growth and lateral mass transport present two evident similarities. First, anisotropic growth only occurs in amorphous targets. Similarly, in this work lateral mass transport is shown to occur in initially crystalline targets only when they have become amorphous. The proposed explanation for this is that, in crystalline materials, if the deformed liquid track is recrystallized by epitaxial growth it will return to its original form, while it can be quenched in its deformed state in an amorphous material. Second, anisotropic growth

is very weak at room temperature, and becomes more important as temperature decreases,[2] similarly, lateral mass transport is not observed at room temperature, while it is observed at liquid-nitrogen temperature. The proposed explanation is that the energetic ion leaves a deformed liquid in its wake. At any temperature, the liquid region will be quenched in a deformed state. At high temperature (even at room temperature), mobile defects in the matrix[13] lead to a relaxation which may bring the material closer to the original, undeformed state. However, if the temperature is low enough to immobilize all defects, then the deformed track would be frozen in. In other words, the accumulation of deformations is prevented. These similarities suggest that lateral mass transport and anisotropic growth are two manifestations of a single basic phenomenon. For irradiation at normal incidence, all the momentum is put in anisotropic growth and, when the ion beam is tilted, the ion momentum component parallel to the surface induces lateral mass transport. Within the momentum transfer model every single ion acts as a little ''hammer,'' thus anisotropic growth would literally be hammering. The connection between lateral mass transport and anisotropic growth was also noticed by Gutzman, Klaumünzer, and Meier,[21] but they attributed these effects to another mechanism, namely viscoelasticity, which will be described in Sec. IV D.

### D. Momentum transfer or viscoelasticity?

Other models have been proposed in the literature to explain deformation phenomena like lateral mass transport and anisotropic growth, such as Coulomb explosions and thermal spikes. The most recent one is the viscoelastic model.[8] In this model, anisotropic growth is explained by the liquefaction of a small cylinder around the ion trajectory followed by thermal expansion of the heated liquid and subsequent relaxation. At least one problem arises with this model. Si (Ref. 22) and InP (Ref. 23) are more dense in their liquid phases than in their solid phases. For example, InP compacts by about 7% when it melts, completely overshadowing the small thermal expansion during the heat-up phase. Therefore the viscoelastic model would predict an anisotropic growth rendering the InP and Si layers thicker, and possibly a lateral transport in the opposite direction (that is, upwind instead of downwind). In both cases, the viscoelastic model gets the sign wrong if the liquidlike phase surrounding the ion track is in fact denser than the crystal.

Furthermore, in the viscoelastic model, the effect of anisotropic growth is described quantitatively by the ''normalized strain rate'' as defined by Trinkaus,[8] which describes the radial growth of the track. Evaluating this quantity for Si and InP, they are expected to behave similarly; however a factor 20 reduction in the mass transport in Si compared to InP is in fact observed.

### V. CONCLUSIONS

Three different phenomena that modify the surface of irradiated solids during irradiation were studied: lateral mass transport, anisotropic growth, and density changes. Various targets were implanted through a steel contact mask. The surfaces were then characterized by atomic force microscopy, surface profilometry, and Auger electron spectroscopy.

Auger spectroscopy was used to verify that the formation of valleys was not due to sputtering of the surface, and that lateral mass transport is not due to surface diffusion effects. Although the three effects cannot be observed independently, the contribution of lateral mass transport has been deduced by using the different windward-downwind symmetries of the effects so that its fluence dependence could be studied. The dependence is linear and the fits for amorphous and crystalline InP both have the same slope (within error bars). For $a$-InP the linear fit crosses the origin, while $c$-InP shows an offset at a fluence of $\approx 10^{14}$ ions/cm$^2$, suggesting that lateral mass transport only begins when the target is amorphous. The fluence dependence was also studied for the irradiation of $a$-InP with 24-MeV Si ions, and, for the irradiation of fused silica, $a$-Si and $a$-Fe$_{40}$Ni$_{40}$B$_{20}$, with 24-MeV Se ions. It was found that lateral mass transport in InP is 5.5 times more effective with Se ions than with Si ions. Among the target materials used, lateral mass transport was the most effective in fused silica and the less effective in $a$-Si.

An estimation of the effect of momentum transfer from the energetic ions to the atoms of the solid for the case of 24-MeV Se ions in $a$-InP showed that if momentum transfer is the only mechanism responsible for lateral mass transport, the atoms in the liquefied track left by the ion must be free to move for about 300 ps. A simple model, based on the deformation of the viscous liquid track by momentum transfer from the incoming ions, to evaluate the energy dependence of the number of displaced atoms by lateral mass transport was also elaborated.

Lateral mass transport and anisotropic growth have very similar features. The effects only occur in amorphous materials and at low temperatures. Both phenomena appear to be two manifestations of the same basic process. We propose that both are a consequence of macroscopic momentum transfer.

[1] R. L. Fleischer, P. B. Price, and R. M. Walker, *Nuclear Tracks in Solids* (University of California Press, Berkeley, 1975).

[2] A. Benyagoub and S. Klaumünzer, Radiat. Eff. **126**, 105 (1993).

[3] A. Audouard, E. Balanzat, G. Fuchs, J. C. Jousset, D. Lesueur,

and L. Thomé, Europhys. Lett. **5**, 241 (1988).

[4] A. Audouard, E. Balanzat, S. Bouffard, J. C. Jousset, A. Chamberod, A. Dunlop, D. Lesueur, G. Fuchs, R. Spohr, J. Vetter, and L. Thomé, Phys. Rev. Lett. **65**, 875 (1990).

[5] Ming-dong Hou, S. Klaumünzer, and G. Schumacher, Phys. Rev. B **41**, 1144 (1990).

[6] M. Toulemonde, C. Dufour, and E. Paumier, Phys. Rev. B **46**, 14 362 (1992).

[7] D. Lesueur and A. Dunlop, Radiat. Eff. **126**, 163 (1993).

[8] H. Trinkaus and A. I. Ryazanov, Phys. Rev. Lett. **74**, 5072 (1995).

[9] L. Cliche, S. Roorda, M. Chicoine, and R. A. Masut, Phys. Rev. Lett. **75**, 2348 (1995).

[10] C. A. Volkert, J. Appl. Phys. **70**, 3521 (1991).

[11] R. S. Averback, T. Diaz de la Rubia, H. Hsieh, and R. Benedek, Nucl. Instrum. Methods Phys. Res. B **59/60**, 799 (1991).

[12] Z. G. Wang, Ch. Dufour, E. Paumier, and M. Toulemonde, J. Phys. Condens. Matter. **6**, 6733 (1994).

[13] L. Cliche, S. Roorda, and R. A. Masut, Appl. Phys. Lett. **65**, 1754 (1994).

[14] C. R. Wie, T. Jones, T. A. Tombrello, T. Vreeland, Jr., F. Xiong, Z. Zhu, G. Burns, and F. H. Dacol, in *Beam-Solid Interactions and Transient Processes*, edited by M. O. Thompson, S. T. Picraux, and J. S. Williams, MRS Symposia Proceedings No. 74 (Materials Research Society, Pittsburgh, 1987), p. 517.

[15] J. S. Custer, M. O. Thompson, D. C. Jacobson, J. M. Poate, S. Roorda, W. C. Sinke, and F. Spaepen, Appl. Phys. Lett. **64**, 437 (1994).

[16] L. C. Feldman and J. W. Mayer, *Fundamentals of Surface and Thin Film Analysis* (Elsevier, New York, 1986).

[17] However even if the electron-phonon coupling is appropriate to describe the behavior of a single electron interacting with a lattice, it may not be appropriate to describe the behavior of electrons around an ion track because of the large density of excited electrons.

[18] S. R. Stiffler, P. V. Evans, and A. L. Greer, Acta Metall. Mater. **40**, 1617 (1992).

[19] M. O. Thompson, J. W. Mayer, A. G. Cullis, H. C. Webber, N. G. Chew, J. M. Poate, and D. C. Jacobson, Phys. Rev. Lett. **50**, 896 (1983).

[20] See, for example, L. D. Landau and E. M. Lifshitz, *Fluid Mechanics* (Pergamon, London, 1959).

[21] A. Gutzmann, S. Klaumünzer, and P. Meier, Phys. Rev. Lett. **74**, 2256 (1995).

[22] *Properties of Si*, edited by C. Hilum (INSPEC, Surrey, 1988).

[23] T. Inada and T. Fukuda, in *Indium Phosphide: Crystal Growth and Characterization*, edited by R. K. Willardson and A. C. Beer, Semiconductors and Semimetals Vol. 31 (Academic, New York, 1990), p. 71.